Journal of Materials Chemistry A

Outstanding thermoelectric properties in solvothermal-synthesized Sn1-3xInxAg2xTe micro-crystals through defect engineering and band tuning

Journal:	*Journal of Materials Chemistry A*
Manuscript ID	TA-ART-10-2019-011614.R2
Article Type:	Paper
Date Submitted by the Author:	n/a
Complete List of Authors:	Moshwan, Raza; The University of Queensland, Materials Engineering Liu, Weidi; The University of Queensland, Materials Engineering Shi, Xiao-Lei; The University of Queensland, Materials Engineering Sun, Qiang; University of Queensland, Gao, Han; University of Queensland Wang, Yun-Peng; Central South University Zou, Jin; The University of Queensland, School of Mechanical and Mining Engineering and Centre for Microscopy and Microanalysis Chen, Zhi-Gang; University of Queensland, School of Mechanical and Mining Engineering; University of Southern Queensland - Springfield Campus, Centre for Future Materials

Journal of Materials Chemistry A
Materials for energy and sustainability

Guidelines for Reviewers

Thank you very much for agreeing to review this manuscript for *Journal of Materials Chemistry A*.

Journal of Materials Chemistry A is a weekly journal in the materials field. The journal is interdisciplinary, publishing work of international significance on all aspects of materials chemistry related to applications in energy and sustainability. Articles cover the fabrication, properties and applications of materials.

Journal of Materials Chemistry A's Impact Factor is **10.733** (2018 Journal Citation Reports®)

The following manuscript has been submitted for consideration as a

FULL PAPER

For acceptance, a Full Paper must report primary research that demonstrates significant **novelty and advance**, either in the chemistry used to produce materials or in the properties/ applications of the materials produced. Work submitted that is outside of these criteria will not usually be considered for publication. The materials should also be related to the theme of energy and sustainability.

When preparing your report, please:

- Focus on the **originality**, **importance**, **impact** and **reproducibility** of the science.
- Refer to the **journal scope and expectations**.
- **State clearly** whether you think the article should be accepted or rejected and give detailed comments (with references) both to help the Editor to make a decision on the paper and the authors to improve it.
- **Inform the Editor** if there is a conflict of interest, a significant part of the work you cannot review with confidence or if parts of the work have previously been published.
- **Provide your report rapidly** or inform the Editor if you are unable to do so.

Best regards,

Professor Anders Hagfeldt
Editor-in-Chief
EPFL, Switzerland

Dr Sam Keltie
Executive Editor
Royal Society of Chemistry

Contact us

Please visit our reviewer hub for further details of our processes, policies and reviewer responsibilities as well as guidance on how to review, or click the links below.

What to do when you review

Reviewer responsibilities

Process & policies

Graphical abstract

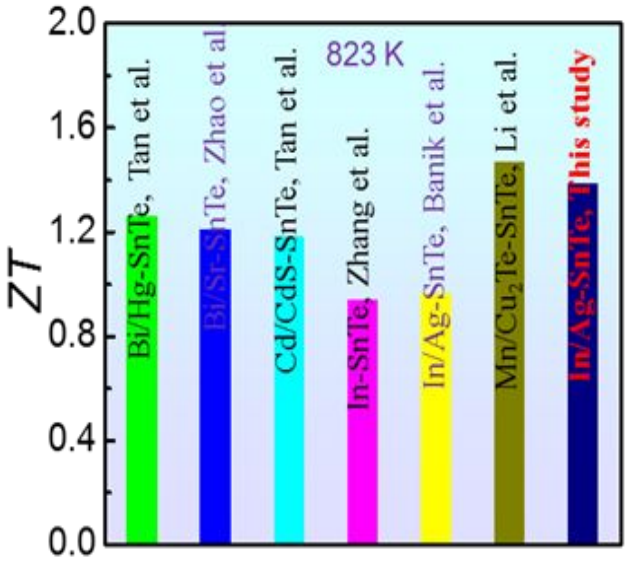

The synergistic effect of resonance energy level and the valence band convergence due to In and Ag co-doping significantly improved the electrical transport properties of $Sn_{1-3x}In_xAg_{2x}Te$, while the defect engineering ameliorated the thermal transport properties to a great extent which make SnTe as an ideal alternative of toxic lead telluride.

Response to comments of Reviewer 3

General Comment*: SnTe is an important TE candidates that can be used in the power generation. In this work, the authors improve its TE performance using In and Ag as co-dopants, and finally raise its highest ZT value to 1.38 at 823 K. This value stands high compared with other works, due to the enhancement in electrical performance and at the same time the reduction in the lattice part κL. This will be of interest to the community of energy materials researchers. Besides, the detailed analysis to the thermoelectric performance has been done and the influence of Ag/In co-doping on thermoelectric performance of SnTe has been realized. Moreover, the authors have carefully revised their manuscript according to the reviewers' comments, which is important for the improvement of the manuscript.*

Indeed, it is true that the SnTe-based system as a thermoelectric candidate has already been studied by many workers in terms of my reviewing of the published articles, even the dopant that they selected in the material system is similar to those reported, such as those in published articles J. Am. Chem. Soc., 2016, 138, 13068 and Proc. Natl. Acad. Sci., 2013, 110, 13261. In view of this, I recommend that the manuscript could be transferred to the JMCC or Dalton Trans.

Response: We appreciate the comments. The papers published in J. Am. Chem. Soc., 2016, 138, 13068 and Proc. Natl. Acad. Sci., 2013, 110, 13261 reported the significant progress in the field of SnTe. However, their synthesis methods were melting which is totally different from our study. Also, their reported *ZT* values was below than the current study (~1.38). Moreover, In/Ag co-doping is very effective approach to enhance the thermoelectric properties of SnTe. Therefore, we believe that our study reports the new approach and in turn produces better SnTe, so that the manuscript is appropriated for publication in the prestigious JMCA.

Response to comments of Reviewer 4

General Comment*: The work by Moshwan et al reports greatly improved thermoelectric performance of the In and Ag co-doped SnTe. The Seebeck coefficient has been significantly increased because of the introduction of resonant level as well as the convergency of valence band. The multiscale microstructures originated from elemental doping and solvothermal synthesis result in substantially decreased lattice thermal conductivity of the material. Thus, a greatly enhanced zT value was finally achieved. The content of the manuscript is interesting and helpful to the thermoelectric society. However, as mentioned by the other reviewers, there are still a large space to improve the manuscript. If the author can well address the following two major concerns, I would like to recommend the publication of this work in JMCA.*

Comment 1*:* The author might not think carefully about the reviewer's previous question about the relationship between the synthesis method and sample composition. The most important point is how the author can precisely control the solvothermal synthesis to obtain the designed sample composition. It is well known that the composition of the sample synthesized by solvothermal method could be not the desired one.

Response: We appreciate the positive comments and constructive suggestions. The achievement of the desired composition in solvothermal method depends critically upon its synthesis parameters, such as temperature and reaction time.[1] In our study, we employed high temperature (230 °C) and long soaked time (24 h), which played a vital role to attain the composition of our final product close to the designed composition.

***Comment 2**:* The second comment is about the design of the sample composition, which has also been questioned by other reviewers. As the author mentioned in the introduction section, the pristine SnTe shows overhigh hole concentration because of large amounts of intrinsic Sn vacancies. Thus, it is generally expected that a sample composition reducing the hole concentration will be designed. However, the author did not intend to decrease the carrier concentration according to the sample composition $Sn_{1-3x}In_xAg2_xTe$ in this work. On the surface at least, the hole concentration shall increase with the doping concentration x for the sample $Sn_{1-3x}In_xAg2_xTe$.

***Response**:* To further clarify this point, we added the following discussion in our revised manuscript at Page 2 as: " To realize the higher solubility of Ag and to avoid rapid decrease in electrical conductivity due to increase in In concentration, an In:Ag ration of 1:2 was chosen, similar to the compositional ratio reported previously [2,3] It should be noted that the solubility limit of the single In dopant in SnTe is <1% and when the amount of In is >1%, the hole concentration of the system and the electrical conductivity significantly decreased, which offset the overall power factor.[4,5] To retain the high power factor, we introduced the In:Ag = 1:2 ratio in this study, which also maximize the resonance effect and the band convergence."

Reference

1. W. Ouyang, A. R. P. Santiago, K. Cerdán-Gómez and R. Luque, in *Photoactive Inorganic Nanoparticles*, eds. J. P. Prieto and M. G. Béjar, Elsevier, 2019, pp. 109-138.
2. D. K. Bhat and U. S. Shenoy, *Mater. Today Phys.*, 2018, **4**, 12.
3. R. Moshwan, W.-D. Liu, X.-L. Shi, Y.-P. Wang, J. Zou and Z.-G. Chen, *Nano Energy*, 2019, **65**, 104056.
4. Q. Zhang, B. Liao, Y. Lan, K. Lukas, W. Liu, K. Esfarjani, C. Opeil, D. Broido, G. Chen and Z. Ren, *Proc. Natl. Acad. Sci.*, 2013, **110**, 13261.
5. R. Moshwan, X.-L. Shi, W.-D. Liu, Y. Wang, S. Xu, J. Zou and Z.-G. Chen, *ACS Appl. Energy Mater.*, 2019, **2**, 2965.

Journal Name

ARTICLE

Outstanding thermoelectric properties in solvothermal-synthesized $Sn_{1-3x}In_xAg_{2x}Te$ micro-crystals through defect engineering and band tuning

Received 00th January 20xx,
Accepted 00th January 20xx

DOI: 10.1039/x0xx00000x

www.rsc.org/

Raza Moshwan,[a,e] Wei-Di Liu,[a] Xiao-Lei Shi,[b,a] Qiang Sun,[a] Han Gao,[a] Yun-Peng Wang,[c] Jin Zou,[d,a,] and Zhi-Gang Chen[b,a,*]*

Due to the eco-friendly nature, tin telluride (SnTe) based thermoelectric materials have attracted extensive attention. Pristine SnTe suffers from low thermoelectric performance because of its large energy separation between two valence bands (heavy hole and light hole) and high thermal conductivity. In this study, we use In and Ag co-dopants to ameliorate the electrical and thermal transport properties of SnTe-based materials using a facile solvothermal method. From the theoretical calculation and performance evaluation, high-level In and Ag co-dopants can significantly converge two valence bands and increase the density of states near the Fermi level, leading to the enhanced Seebeck coefficient from ~95 μVK^{-1} in the pristine SnTe to ~178 μVK^{-1} in the $Sn_{0.85}In_{0.05}Ag_{0.10}Te$. Comprehensive structural characterization shows that high-density strain fields and dislocations exist in the sintered pellets, together with the point defects, and grain boundaries secured remarkably low lattice thermal conductivity of SnTe in the entire temperature range. As a result, a high peak figure of merit of ~1.38 at 823 K has been achieved in $Sn_{0.85}In_{0.05}Ag_{0.10}Te$, outperforming most of SnTe-based materials. This study indicates that co-doping with high solubility can simultaneously tune band structure and engineer defects for achieving enhanced thermoelectric performance of SnTe-based materials.

Introduction

Thermoelectric materials, enabling to covert heat directly into electricity, has been considered as an alternative solution to utilize large-scale waste heat emanated from industrial and automotive sectors.[9-14] As a sustainable and eco-friendly energy technology, thermoelectric generators offer zero pollution, no moving parts and high durability. The thermoelectric conversion efficiency of a material is determined by the dimensionless figure of merit, *ZT*, defined as

$$ZT = \frac{S^2\sigma}{\kappa}T = \frac{S^2\sigma}{\kappa_e + \kappa_l}T \quad (1)$$

where σ is the electrical conductivity, S is the Seebeck coefficient, κ is thermal conductivity, T is the absolute temperature, κ_e and κ_l are the electrical and lattice thermal conductivities. The strong interdependence among S, σ, and κ_e challenge the concurrent rise in the power factor ($S^2\sigma$) and the reduction in κ. Several strategies have been executed to enhance *ZT* of thermoelectric materials, including convergence of electronic bands,[15-20] carrier concentration optimization,[21-24] nanostructuring,[25-31] quantum confinement,[32, 33] all-scale hierarchical architecturing,[34-37] phonon-phonon interaction,[39] defects engineering,[40, 41] lattice anharmonicity[25, 42-44] and porous design.[45-47]

Among different types of thermoelectric materials, eco-friendly SnTe has received extensive attention as an alternative for toxic PbTe.[9, 42, 48, 49] SnTe possesses similar crystal and electronic structures with PbTe.[9] However, SnTe has much higher lattice thermal conductivity than PbTe at the room temperature attributed to the much lighter atomic mass of Sn (118 amu) than Pb (207 amu).[1] Besides, the energy separation between two valence bands in SnTe (~0.3-0.4 eV) is significantly higher than that in PbTe,[1] leading to a low S of the pristine SnTe. Due to the high concentration of intrinsic Sn vacancies, the high hole carrier concentration (n, ~10^{20} to 10^{21} cm^{-3}) is another inferior factor for the electronic and thermal transport of the pristine SnTe. Several strategies have been used to improve the electrical transport properties of SnTe. For instance, Banik *et al.*[50, 51] introduced Mg and Ag dopants to reduce the energy separation between two valence bands. Tan *et al.*[4, 8] studied the valence band convergence caused by Hg and Cd doping. Zhang *et al.*[2] first studied the resonance states introduced by In dopants in SnTe. Both band convergence and resonant states lead to the S enhancement. Moreover, the synergistic

[a] Materials Engineering, The University of Queensland, St Lucia, QLD 4072, Australia.
[b] Centre for Future Materials, The University of Southern Queensland, Springfield Central, QLD 4300, Australia.
[c] School of Physics and Electronics, Hunan Key Laboratory for Super-micro structure and Ultrafast Process, Central South University, 932 South Lushan Road, Changsha, P. R. China.
[d] Centre for Microscopy and Microanalysis, The University of Queensland, St Lucia, QLD 4072, Australia.
[e] University of Creative Technology Chittagong, Chandgaon Police Station, 1084, Shah Amanat Bridge Connecting Road, Chittagong 4212, Bangladesh

Electronic Supplementary Information (ESI) available: [details of any supplementary information available should be included here]. See DOI: 10.1039/x0xx00000x

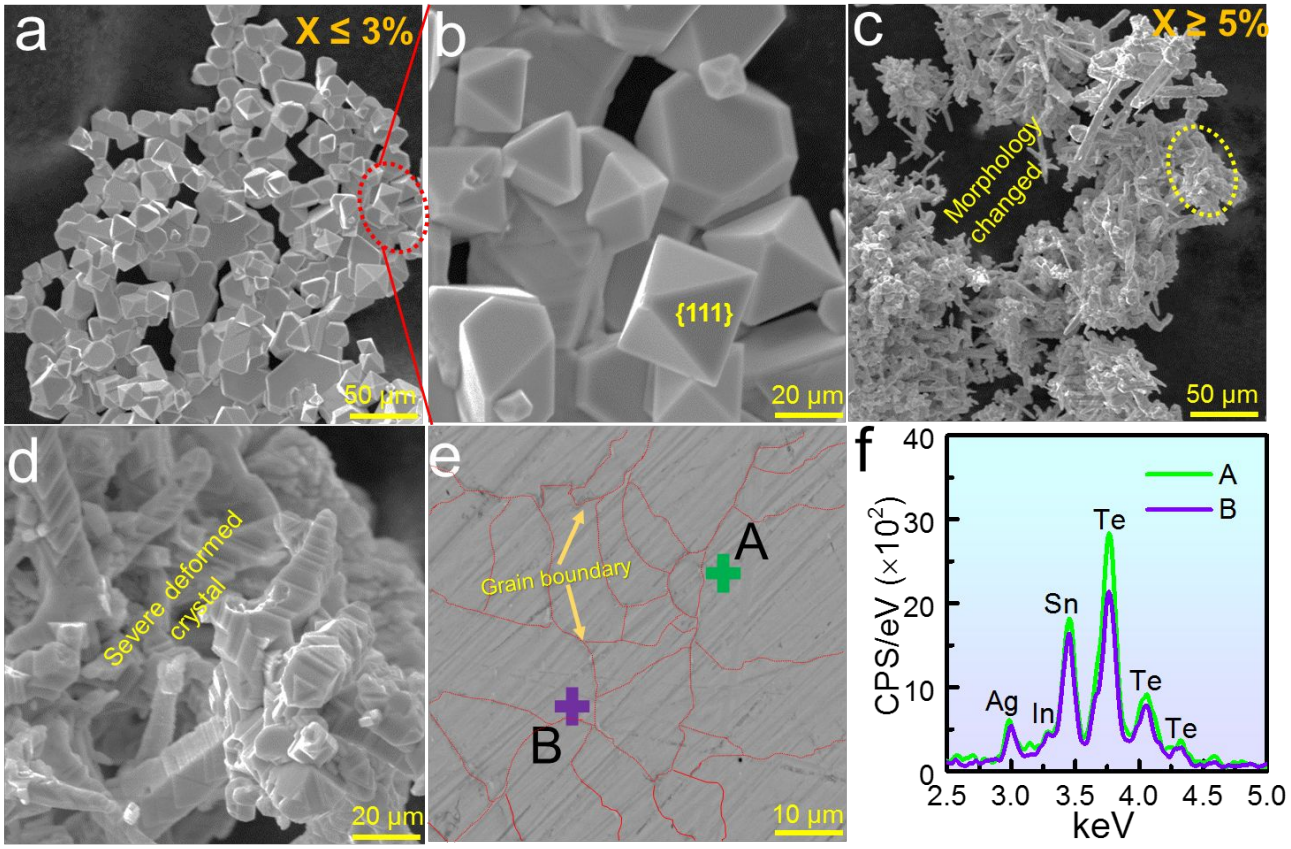

Figure 1. (a) Typical SEM micrograph of $Sn_{1-3x}In_xAg_{2x}Te$ ($x \leq 3$ %) powders (b) Enlarged image of highlighted area of (a) shows the regular {111} planes of as-synthesized crystal. (c) SEM micrograph of $Sn_{1-3x}In_xAg_{2x}Te$ ($x \geqslant 5$ %) powders (d) Enlarged image of highlighted area of (c) shows severe deformation of regular crystal shapes (e) A typical SEM image of the sintered $Sn_{0.85}In_{0.05}Ag_{0.10}Te$ pellet (f) Corresponding EDS spectrums of spot A and B of (e), showing significant peaks of Sn, Te, In and Ag.

engineering of valence band convergence and resonance states has been realized in a few co-doped SnTe systems, such as In/Cd,[6, 49] In/Mg,[52] In/Mn,[53] In/Hg,[54] In/Ca[55] and In/Sr.[48] A recent study on In/Ag co-doped SnTe fabricated by conventional melting method showed an enhanced peak *ZT* of ~ 1 at x = 2.5 % in $SnIn_xAg_xTe_{1+2x}$.[5] The observed κ_l values for all $SnIn_xAg_xTe_{1+2x}$ samples are always higher than the pristine SnTe, which offsets the overall *ZT* enhancement.

In this study, we use a facile and low cost solvothermal method to synthesize $Sn_{1-3x}In_xAg_{2x}Te$ (x = 0, 1.0 %, 3.0 %, 5.0 %, and 6.0 %) micro-sized crystals. To realize the higher solubility of Ag and to avoid rapid decrease in electrical conductivity due to increase in In concentration 1:2 (In:Ag) was chosen. Similar compositional ratio have been reported in the previous work by Bhat *et al*. [55] and Moshwan *et al*..[48] It should be noted that the solubility limit of the single In dopant in SnTe is <1% and when the amount of In is >1%, then the hole concentration of the system and the electrical conductivity significantly decreased which offset the overall power factor.[2, 42] In order to retain the high power factor we introduced In:Ag as 1:2, which also maximize the resonance effect and the band convergence.Through systematic first-principles density functional theory (DFT) calculations, we found that In and Ag dopants lead to synergistically resonant states and valence band convergence, leading to remarkable enhancement in $S^2\sigma$ of $Sn_{1-3x}In_xAg_{2x}Te$ (x > 0%). Moreover, high density strain field and dislocations can be observed in the sintered $Sn_{1-3x}In_xAg_{2x}Te$ pellets (x > 5 %), which together with the point defects, and grain boundaries leading to intensive scattering of phonons and in turn yield ultra-low lattice thermal conductivity in a wide temperature range. Consequently, a peak *ZT* of ~1.38 has been achieved in $Sn_{1-3x}In_xAg_{2x}Te$ at 823 K, which outperforms most of the reported SnTe-based materials at the similar temperature.

Results and discussion

Figure 1a and b are typical SEM images of as-synthesized $Sn_{1-3x}In_xAg_{2x}Te$ (x ≤3 %) powders, and show that the products are octahedral-shape micro-sized crystals. **Figure 1**c and d are SEM images of as-synthesized $Sn_{1-3x}In_xAg_{2x}Te$ (≥5 %,) severely deformed micro-sized crystals. **Figure 1**e shows a SEM image of a sintered $Sn_{0.85}In_{0.05}Ag_{0.10}Te$ pellet (as an example) in which small grains and grain boundaries can be seen in the sintered pellet, as indicated by orange arrows. In order to determine the compositions of the pellets, we performed EDS analyses and the typical results are shown in **Figure 1f**. After the statistically quantitative analysis, all these pellets have the similar compositions with the nominal values of the solvothermal-synthesis products. The corresponding EDS profiles and

quantitative analyses data are shown in **Figure S3** of the supporting information. We provided an elemental map analysis of x = 5 % sample in **Figure S4**. It is obvious that the composition of Sn, Te, In and Ag is uniform.

the measured n and the calculated μ of the sintered $Sn_{1-3x}In_xAg_{2x}Te$ pellets, in which the room-temperature n does not fluctuate much with increasing the In/Ag doping concentration, due to the electron donor acceptor behaviour of In and Ag atoms. Room-temperature μ decreases gradually with

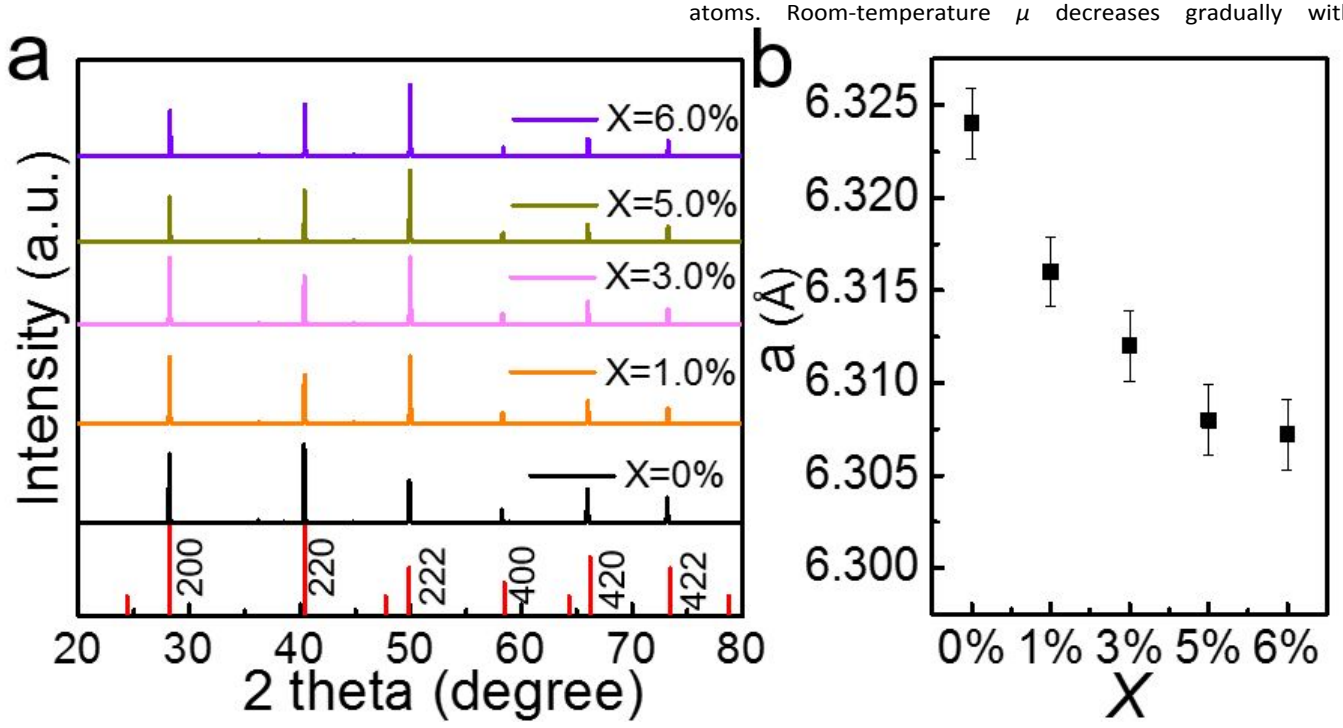

Figure 2. (a) XRD patterns of the sintered $Sn_{1-3x}In_xAg_{2x}Te$ (x = 0 %, 1.0 %, 3.0 %, 5.0 % and 6 %) pellets. (b) Calculated lattice parameter with the respect of In/Ag co-doping concentration.

Figure 2a shows the XRD patterns of the sintered $Sn_{1-3x}In_xAg_{2x}Te$ (x = 0%, 1.0 %, 3.0 %, 5.0 %, and 6.0 %) pellets, in which the diffraction peaks can be inclusively indexed as the FCC structured SnTe (standard identification card, PDF #65−0239, the pink line in **Figure 2**a) with a lattice parameter of a = 6.32 Å and a space group of $Fm\bar{3}m$. No secondary phases were identified within the detectability limits, indicating a high solubility of In and Ag co-doping in SnTe when comparing with the reported results.[56] As shown in the calculated lattice parameter of the sintered $Sn_{1-3x}In_xAg_{2x}Te$ ((x = 1.0 %, 3.0 %, 5.0 %, and 6.0 %)) pellets (**Figure 2**b), the rate of the decreased lattice parameter is relatively high with increasing the In/Ag co-doping concentration from x = 0 % up to x = 5 % while the lattice parameter is almost stable at x = 6 %, suggesting that the In/Ag co-doping is approaching to the solubility limit. It should be noted that the decrease in the lattice parameter is attributed to the smaller ionic radius of In^{3+} (80 pm) and Ag^{+1} (115 pm) when compared with Sn^{2+} (118 pm). **Figure S5** shows the extended XRD peaks (200) planes and demonstrate the peaks are shifting towards higher angle confirming the lattice shrinkage after In/Ag co-doping.

Figure 3 shows the temperature-dependent electrical transport properties of sintered $Sn_{1-3x}In_xAg_{2x}Te$ (x = 0 %, 1.0 %, 3.0 %, 5.0 % and 6 %) pellets. As shown in **Figure 3a**, the inherent high σ of pristine SnTe is gradually reduced with increasing the In/Ag co-doping content. At 300 K, σ of pristine SnTe is ~7240 S cm^{-1}, and is decreased to ~2811 S cm^{-1} for x = 6 %. **Figure 3b** shows increasing x from 0 % to 6 % (**Figure 3b**). For example, room-temperature μ reduces from ~70 $cm^2V^{-1}s^{-1}$ of pristine SnTe to ~30 $cm^2V^{-1}s^{-1}$ of $Sn_{1-3x}In_xAg_{2x}Te$ at x = 6%. The decrease in μ should be attributed to the higher effective mass (m^*) of the carriers from the heavy hole valence band, which further is verified by the calculation from a single parabolic band model. m^* can be determined using the following equations,[45]

$$S(\eta) = \frac{k_B}{e} \cdot \left[\frac{\left(r+\frac{5}{2}\right) \cdot F_{r+\frac{3}{2}}(\eta)}{\left(r+\frac{3}{2}\right) \cdot F_{r+\frac{1}{2}}(\eta)} - \eta \right] \quad (2)$$

$$n_H = \frac{1}{e \cdot R_H} = \frac{(2m^* \cdot k_B T)^{\frac{3}{2}}}{3\pi^2\hbar^3} \cdot \frac{\left(r+\frac{3}{2}\right)^2 \cdot F^2_{r+\frac{1}{2}}(\eta)}{(2r+\frac{3}{2}) \cdot F_{2r+\frac{1}{2}}(\eta)} \quad (3)$$

where η, k_B, e, r, R_H, and $\hbar$ are the reduced Fermi level, Boltzmann constant, electron charge, carrier scattering factor (r = -1/2 for acoustic phonon scattering), Hall coefficient, effective mass, and reduced plank constant, respectively. $F_i(\eta)$ is the Fermi integral express as

$$F_i(\eta) = \int_0^\infty \frac{x^i}{1+e^{(x-\eta)}} dx \quad (4)$$

Figure 3c shows the determined m^* as a function of x, in which m^* increases from 0.87 m_0 of the pristine SnTe (x = 0%) to 2.78 m_0 of $Sn_{1-3x}In_xAg_{2x}Te$ for x = 6%, indicating that the heavy hole contribution to the electron hole transportation from valence band to conduction band in $Sn_{1-3x}In_xAg_{2x}Te$. We also estimated

the room-temperature deformation potential (E_{def}) of $Sn_{1-3x}In_xAg_{2x}Te$, and the results are shown in **Figure 3**d. The relationship between E_{def} and μ can be expressed as[45]

$$\mu_H = \left[\frac{e\pi\hbar^4 \quad C_l}{\sqrt{2}(k_BT)^{\frac{3}{2}}E_{def}{}^2(m^*)^{\frac{5}{2}}}\right]\frac{(2r+\frac{3}{2})\cdot F_{2r+\frac{1}{2}}(\eta)}{\left(r+\frac{3}{2}\right)^2\cdot F_{r+\frac{1}{2}}(\eta)} \quad (5)$$

near the Fermi level in the valence according to the following equation $S=\frac{\pi^2k_B}{3q}k_BT\left[\frac{g(E)}{n(E)}+\frac{1}{\mu E}\frac{d\mu(E)}{dE}\right]$, where q is the electron charge, $k_B$is the Boltzmann constant, and $g(E)$ is the DOS.[42] S steadily increases with increasing the temperature for all $Sn_{1-3x}In_xAg_{2x}Te$ (x >0 %). The contribution of heavy mass carrier from the second sub-band manifests S.

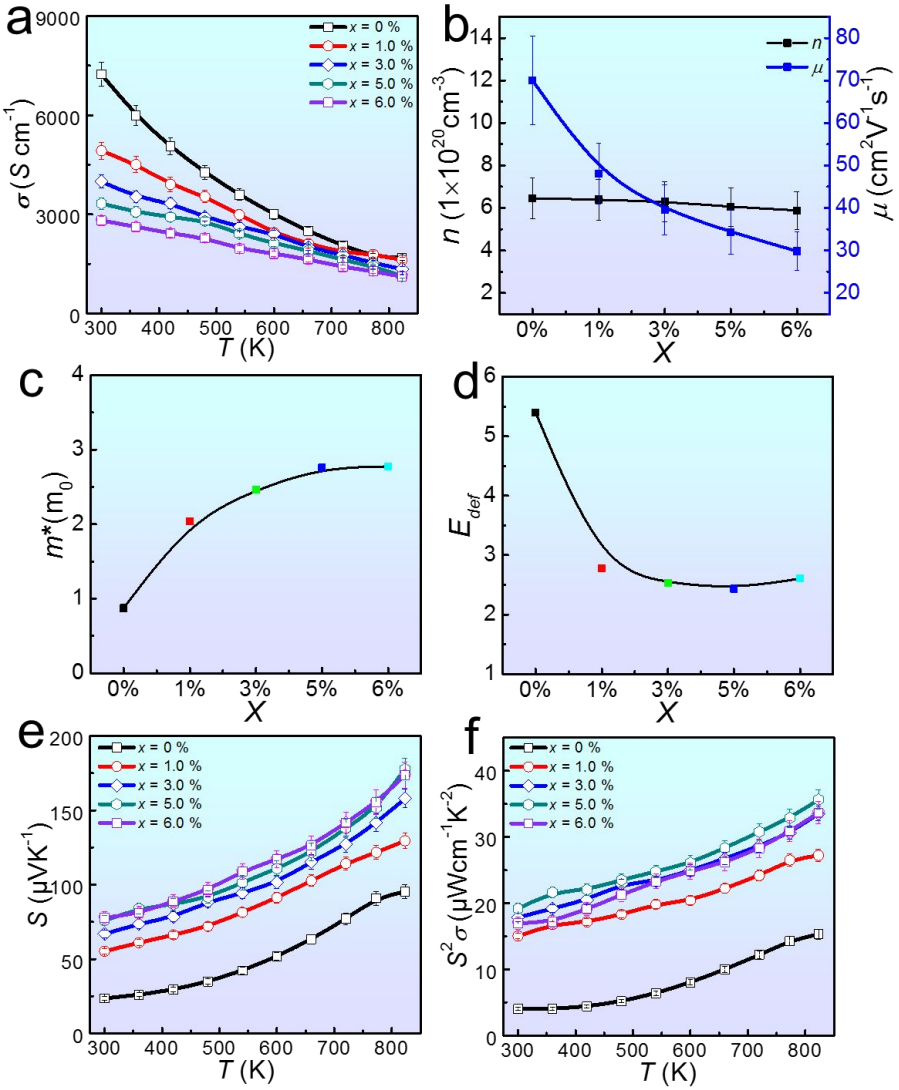

Figure 3. Electrical transport properties of sintered $Sn_{1-3x}In_xAg_{2x}Te$ (x = 0 %, 1.0 %, 3 %, 5 %, and 6 %,) samples: (a) σ, (b) n and μ, (c) m^* (d) E_{def} (e) S, (f) $S^2\sigma$. (error bar 5 %)

where C_l ($C_l = v_l^2 \cdot \rho$, v_l and ρ are the longitudinal sound velocity and density) elastic constant for longitudinal vibrations. The v_l was taken as 3371 ms^{-1} As shown in **Figure 3**d, E_{def} of all $Sn_{1-3x}In_xAg_{2x}Te$ (x > 0%) are lower than the pristine SnTe, theoretically suggesting the enhanced μ. However, the higher m^* offsets the influence of reduction in E_{def}.[45]

Figure 3e shows the temperature-dependent S of the sintered $Sn_{1-3x}In_xAg_{2x}Te$ (x = 0 %, 1.0 %, 3.0 %, 5.0 % and 6 %) pellets, in which S of the In/Ag co-doping SnTe is higher than that of the pristine SnTe in the entire temperature range. For instance, the room-temperature S of x = 5 % is ~178 μVK^{-1} which is ~1.9 times higher than that of pristine SnTe, due to the significant valence band convergence and resonance energy level caused by the In/Ag co-doping. The resonance effect leads to increases in DOS

Figure 3f shows the calculated temperature-dependent $S^2\sigma$ of the sintered $Sn_{1-3x}In_xAg_{2x}Te$ (x = 0 %, 1.0 %, 3.0 %, 5.0 % and 6 %) pellets. The $S^2\sigma$ values of In/Ag co-doped SnTe are well above than that of the pristine SnTe due to the significant S enhancement. Specifically, room-temperature $S^2\sigma$ considerably increases from ~4.04 $\mu Wcm^{-1}K^{-2}$ of the pristine SnTe to ~19.18 $\mu Wcm^{-1}K^{-2}$ of $Sn_{0.85}In_{0.05}Ag_{0.10}Te$. A peak $S^2\sigma$ of ~35.67 $\mu Wcm^{-1}K^{-2}$ is obtained for $Sn_{1-3x}In_xAg_{2x}Te$ (x = 5 %) at 823 K.

In order to understand the underlying mechanism of the improved electrical transport properties of $Sn_{1-3x}In_xAg_{2x}Te$ pellets, we carried out theoretical calculation. **Figure 4**a, b, c, and d show the spectra functions for four systems, namely, the pristine SnTe, $Sn_{0.95}In_{0.05}Te$, $Sn_{0.90}Ag_{0.10}Te$ and $Sn_{0.85}In_{0.05}Ag_{0.10}Te$, respectively. The spectra function of the

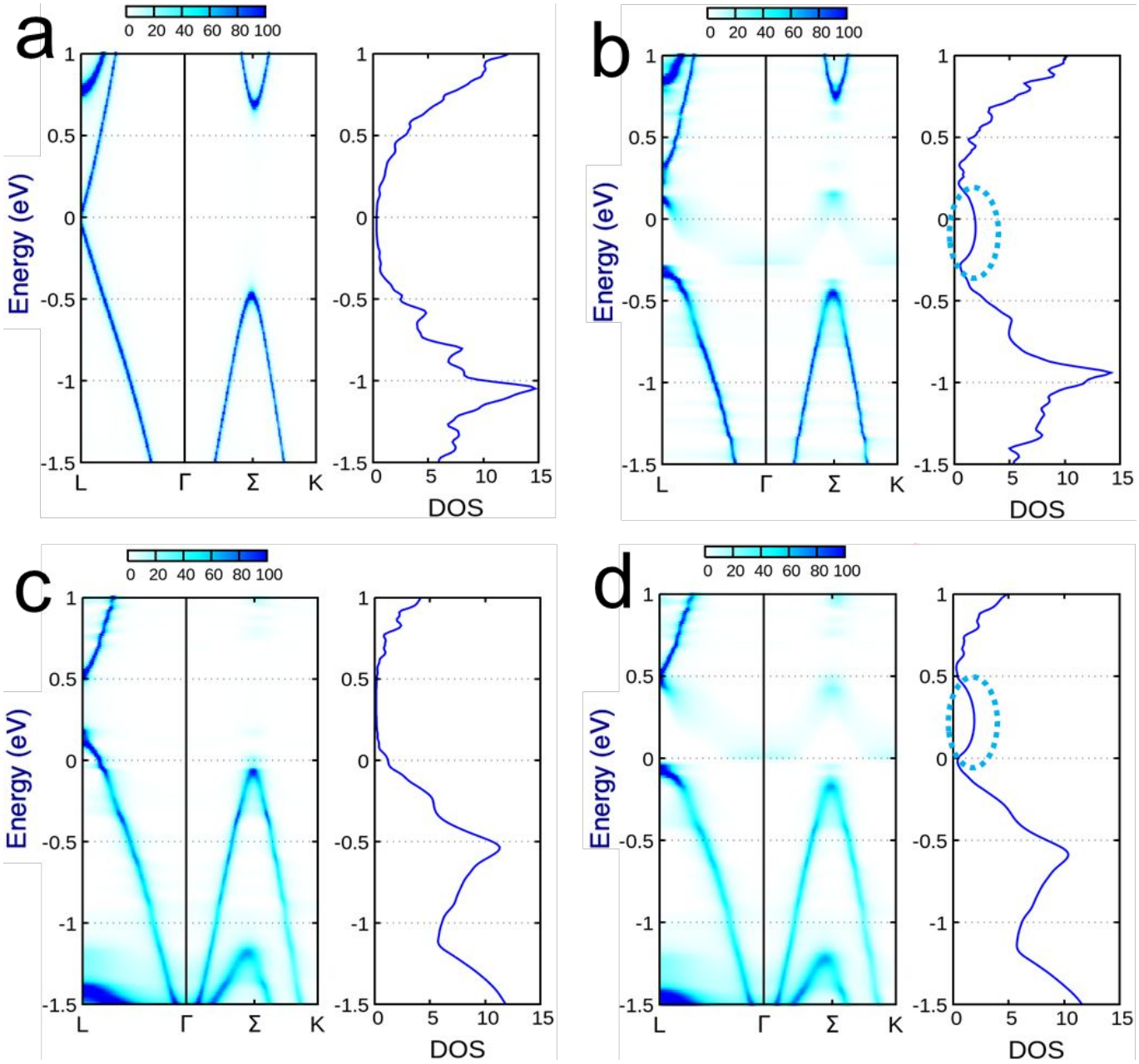

Figure 4. The spectra functions (left panels) and the density of states (right panels) of pristine and doped SnTe. (a) Pristine SnTe, (b) $Sn_{0.95}In_{0.05}Te$, (c) $Sn_{0.90}Ag_{0.10}Te$ and (d) $Sn_{0.85}In_{0.05}Ag_{0.10}Te$.

pristine SnTe exhibits well-defined peaks. The positions of the peaks in the spectra function correspond to the ordinary band structure. For SnTe doped by foreign elements, the peaks in the spectra function are no longer well-defined, but are smeared due to the on-site disorders caused by the atomic substitutions. The spectra function with energies -0.3 eV to 0.2 eV in $Sn_{0.95}In_{0.05}Te$ (**Figure 4**b) and 0 eV to 0.5 eV in the $Sn_{0.85}In_{0.05}Ag_{0.10}Te$ (**Figure 4**d) are too severely smeared to interpret as a band. The spectra function in other energy ranges can still be interpreted as bands. For example, the valence band edge of $Sn_{0.95}In_{0.05}Te$ is at -0.3 eV, and the conduction band edge of $Sn_{0.85}In_{0.05}Ag_{0.10}Te$ is at 0.5 eV.

The substitution by Ag dopants induces p-type doping as indicated by the shifting towards higher energy of the entire band structure. **Figure 4**c shows enhanced energy band gap. The band structure in In-doped SnTe is more complex. Although the band edge at the L point is shifted downwards in the energy scale, the energy of the band edge at the Σ point remains unchanged, as shown in **Figure 4**b. Therefore, little p-type doping is induced by In dopants. The most significant modification in the electronic structure brought by In dopants is the enhanced density of states within an energy range of 0.5 eV around the Fermi energy. The enhanced DOS corresponds to a severely smeared band-like feature in the spectra function, whose energy dispersion near the L and Σ points is parallel with the well-defined valence band below it (**Figure 4**b). In/Ag co-doped SnTe, as shown in **Figure 4**d, exhibits both the p-type

doping due to Ag and the enhanced DOS above the valence band due to In dopants.

even more significant. The energy difference is reduced to 0.15 eV by 5% In dopants. Co-doping by In and Ag produces a larger

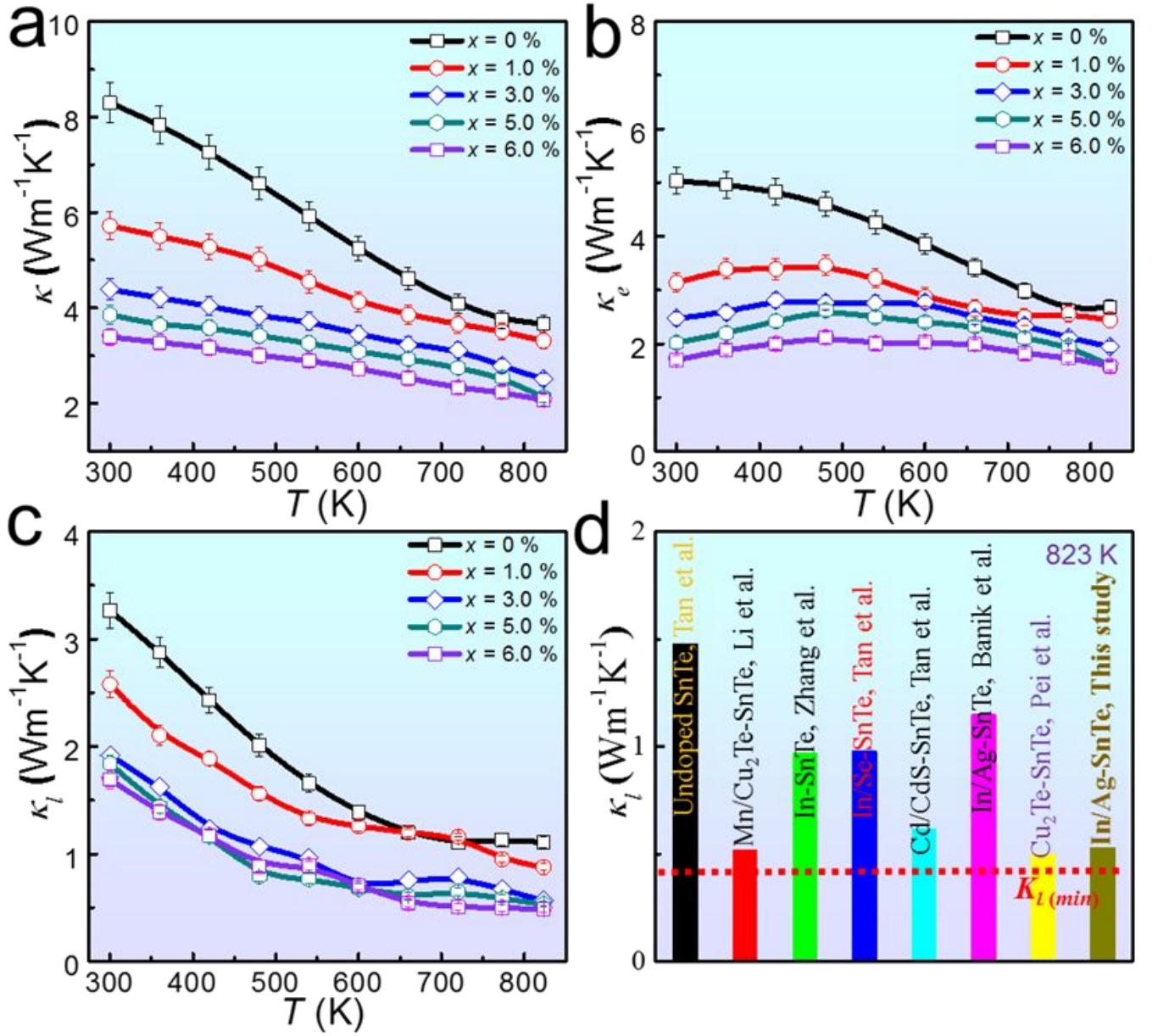

Figure 5. Temperature-dependent thermal transport properties of sintered $Sn_{1-3x}In_xAg_{2x}Te$ (x = 0 %, 1.0 %, 3.0 %, 5.0 %, 6.0 %) samples (error limit is 5 %) (a) κ, (b) κ_e (c) κ_l. (error limit is 5 %) (d) Comparison of current κ_l with the reported results.[1-7]

The enhancement in DOS induced by In dopants is referred to the resonant states.[2] The resonant states result from the strong hybridization between the impurity (In dopant) energy levels and the bands from the matrix material (SnTe). The severe smearing of spectra functions near the Fermi energy as shown in **Figure 4**b, providing the evidence for the impurity-matrix hybridizations. The band convergence effect is also visible in the calculated spectra functions. The band convergence refers to the reduction of the energy difference between the valence band edges at the L point and at the Σ point. Ag-dopants induce a sizable band convergence effect by reducing the energy difference from 0.42 eV in pristine SnTe to 0.2 eV in $Sn_{0.90}Ag_{0.10}Te$. The band convergence effect by In dopants is band convergence than the single doped. The energy difference is 0.1 eV in $Sn_{0.85}In_{0.05}Ag_{0.10}Te$ (**Figure 4**d). Therefore, we believe that the significant S enhancement observed in the In/Ag co-doped SnTe is attributed to the synergy of band convergence, band gap enlargement and the resonant states.

Figure 5a plots the temperature-dependent κ of the sintered $Sn_{1-3x}In_xAg_{2x}Te$ (x = 0 %, 1.0 %, 3.0 %, 5.0 % and 6 %) pellets, and shows that κ gradually decreased with increasing x value (In/Ag content) in whole temperature range from 300 to 823 K. Room-temperature κ is significantly reduced from ~8.5 W m^{-1} K^{-1} in the pristine SnTe to ~3.39 W m^{-1} K^{-1} in $Sn_{0.82}In_{0.06}Ag_{0.12}Te$. A minimum κ of ~2.07 W m^{-1} K^{-1} at 823 K is obtained in $Sn_{0.82}In_{0.06}Ag_{0.12}Te$, which is 44 % lower than that in the pristine

SnTe at 823 K. **Figure 5b** shows the calculated κ_e of $Sn_{1-3x}In_xAg_{2x}Te$ samples using Wiedemann-Franz law $\kappa_e = L\sigma T$,[57] where L is the Lorenz number, and can be calculated by the following relationship:

$$L = 1.5 + \exp\left(-\frac{|S|}{116}\right) \quad (6)$$

remarkably reduced with increasing the In/Ag doping concentration. The room-temperature κ_l value is greatly reduced from ~3.4 $Wm^{-1}K^{-1}$ in the pristine SnTe to ~1.69 $Wm^{-1}K^{-1}$ in $Sn_{0.82}In_{0.06}Ag_{0.12}Te$. A lowest κ_l of ~0.48 $Wm^{-1}K^{-1}$ is observed in $Sn_{0.82}In_{0.06}Ag_{0.12}Te$ at 823 K. This value is

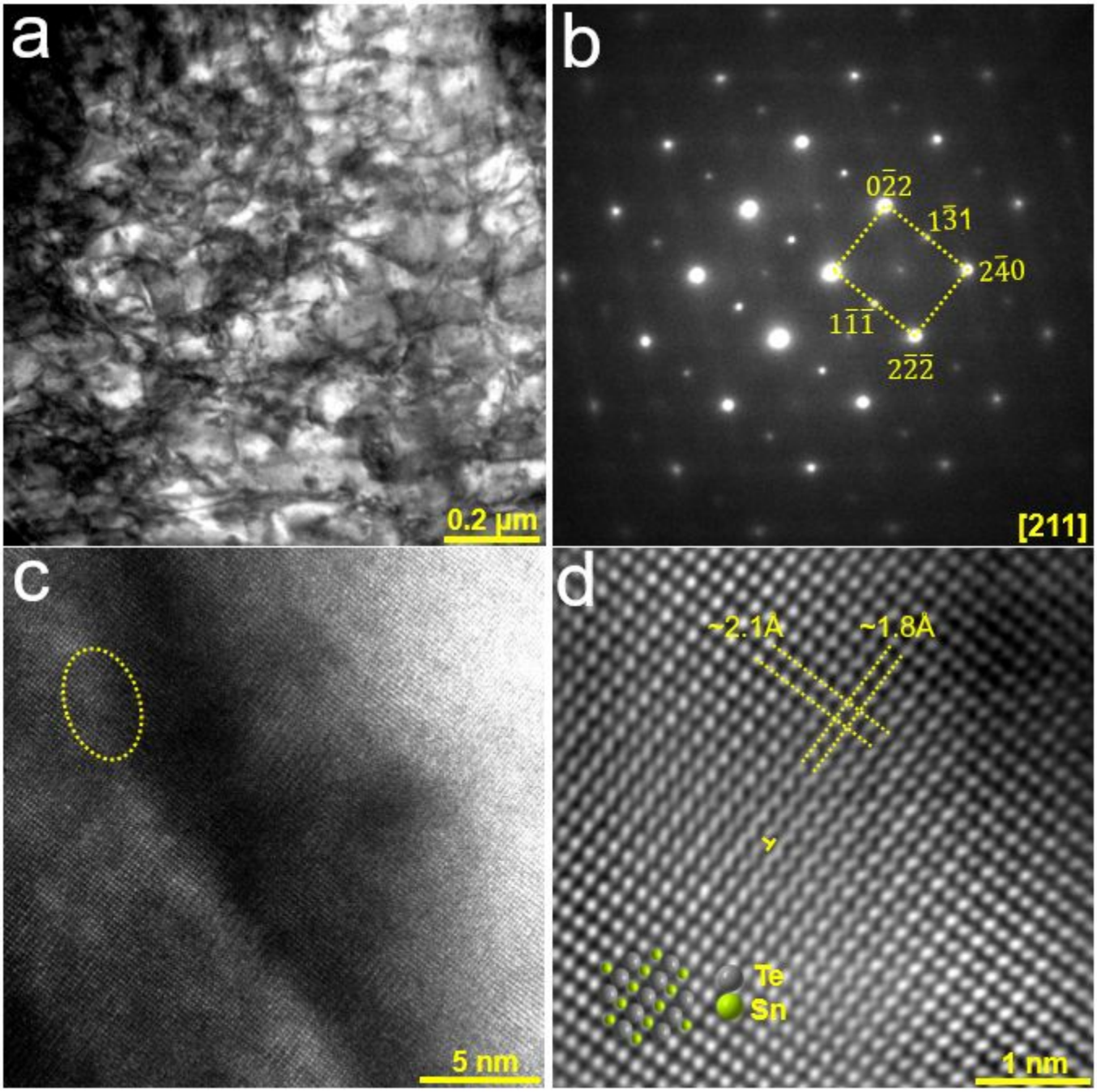

Figure 6. (a) Typical bright field TEM image of $Sn_{0.85}In_{0.05}Ag_{0.10}Te$ sintered pellet shows high density strain field in the matrix. (b) Selected area electron diffraction (SAED) pattern along [211] zone-axis. (c) High resolution transmission electron microscopy image of one strain field area, (d) Magnified image of highlighted area of (c) shows dislocation exist in the matrix.

The calculated L values are well laying in between the Sommerfeld value of degenerated limit (L_{DEG} = 2.45×10^{-8} ΩWK^{-2}) and non-degenerate limit (L_{N-D} = 1.49×10^{-8} ΩWK^{-2})[58] (**Figure S6**). We further calculated κ_l by subtracting κ_e from κ, and the results are shown in **Figure 5c**. Clearly, the κ_l values are approaching to the amorphous limit (~ 0.4 $Wm^{-1}K^{-1}$).[7] **Figure 5d** shows the comparison between our determined κ_l and the reported values, in which our κ_l value is significantly lower than most of the reported κ_l values, including undoped SnTe (melting),[6] Mn/Cu_2Te doped (melting),[1] Cu_2Te doped,[7] In doped

(ball milling),[2] In/Se doped (melting),[3] Cd/CdS doped (melting)[4] and In/Ag doped (melting)[5] SnTe systems, indicating the efficacy of our synthesis method to secure high-performance thermoelectric materials.

In this study, we demonstrated that high thermoelectric properties can be achieved in the In/Ag co-doped SnTe through comprehensive DFT electronic structure calculations, synthesis and structural and composition characterizations. The high-

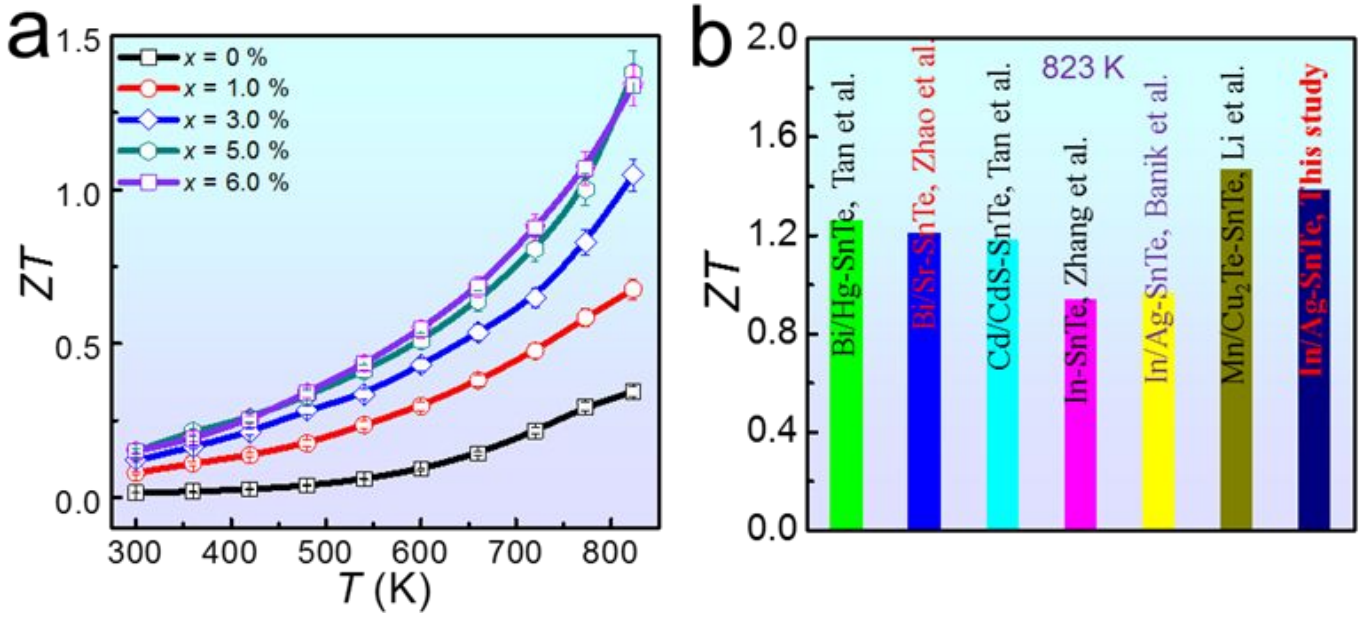

Figure 7. (a) Temperature-dependent (a) *ZT* values of $Sn_{1-3x}In_xAg_{2x}Te$ (x = 0 %, 1.0 %, 3.0 %, 5.0 %, 6.0 %) samples (error limit is 5 %) (b) Comparing current *ZT* value with some of the previously reported results, including Bi/Hg,[8] Bi/Sr,[38] Cd/CdS,[4] In,[2] In/Ag[5] and Mn/Cu_2Te[1] doped SnTe system at 823 K.

To understand the origin of the κ_l reduction in $Sn_{1-3x}In_xAg_{2x}Te$, we performed transmission electron microscopy analyses. **Figure 6**a is a typical bright-field TEM image of $Sn_{0.85}In_{0.05}Ag_{0.10}Te$, in which high density of strain field are exist in the matrix. **Figure 6b** shows the selected area electron diffraction (SAED) pattern along [211] zone axis. A high-resolution transmission electron microscopy (HRETEM) image is shown in **Figure 6c**. The magnified image of highlighted elliptical circle area of **Figure 6c** shows dislocations are exist in the matrix (**Figure 6d**). These strain field, dislocations in the matrix, together with the point defects and grain boundaries significantly scatter heat carrying phonons in all scale and responsible to reduce κ_l to a great extent.

Figure 7a shows the calculated *ZT* of the $Sn_{1-3x}In_xAg_{2x}Te$ pellets, in which the peak *ZT* outstandingly enhanced from 0.34 in the pristine SnTe to 1.38 in $Sn_{0.85}In_{0.05}Ag_{0.10}Te$ at 823 K, which is attributed to the synergistic increase in $S^2\sigma$ and decrease in κ. This *ZT* enhancement is over 4 times higher than that of the pristine SnTe. We also compare our result with some of the previously reported results, including Bi/Hg,[8] Bi/Sr,[38] Cd/CdS,[4] In,[2] In/Ag,[5] Mn/Cu_2Te[1] doped SnTe systems. As can be seen, our *ZT* value outperforms most of the reported (**Figure 7b**), indicating a great potential of In/Ag co-doping with a ratio of 1:2 to achieve significant enhancement in electrical and thermal transport properties of SnTe systems. The synergistic defect engineering and band tuning can be a crucial strategy to obtain high-performance thermoelectric materials.

Conclusions

concentration In and Ag dopants induce resonant states, valence band convergence and band gap enlargement, leading to the enhanced *S* from ~95 μVK^{-1} in the pristine SnTe to ~178 μVK^{-1} in the $Sn_{0.85}In_{0.05}Ag_{0.10}Te$. The co-existence of point defects, strain field, dislocations and grain boundaries significantly reduced lattice thermal conductivity over a wide temperature range. Consequently, an outstanding peak *ZT* of ~1.38 was obtained in $Sn_{0.85}In_{0.05}Ag_{0.10}Te$ that is ~3.06 times higher than that in the pristine SnTe. This study reveals a promising pathway to achieve high-performance thermoelectric materials *via* synergistic band tuning and defect engineering by a facile solvothermal method.

Experiment

Materials synthesis

A facile solvothermal method was used to synthesize $Sn_{1-3x}In_xAg_{2x}Te$ (x = 0%, 1.0 %, 3.0 %, 5.0 %, and 6.0 %) samples. Na_2TeO_3 (99.99%), $SnCl_2{\cdot}2H_2O$ (99.99%), $AgNO_3$ (≥ 99.99%), $InCl_3{\cdot}4H_2O$ (97%), supplied by Sigma-Aldrich, were used as sources of Te, Sn, Ag and In. Ethylene glycol (99.8%) and NaOH (99.99%) were used as solvents to dissolve precursors. The solution was put into a teflon jar, and stirred by magnetic stirrer for several minutes. These teflon jars were then put into stainless-steel autoclaves and sealed to put into a CSK thermal oven, then heated to 230 °C and soaked for 24 h. After that, the synthesized products were collected in centrifuging tubes at room temperature. Absolute ethanol and deionized water were used for centrifuging until the appearance of the clear solution.

Once the centrifuging was completed, the synthesized crystals were dried at 60 °C for 12 h.

Thermoelectric property measurements

The synthesized powders were sintered to form pellets using a spark plasma sintering (SPS) machine under a high vacuum. The pressure, temperature and time for SPS were set as 50 MPa, 823 K and 5 minutes, respectively. In order to measure the thermoelectric properties of the sintered samples, different-grade grind papers were used to polish the sintered pellets. Thermoelectric transport properties, such as Seebeck coefficient and electrical resistivity were simultaneously measured by ZEM-3 (ULVAC) under a helium atmosphere from room temperature to 823 K. Thermal transport properties, such as thermal diffusivity (D), were measured by a laser flash diffusivity method with an LFA 457 (NETZSCH) in the temperature range of 300 to 823 K (**Figure S1**). Specific heat capacity, C_p was measured by DSC 404 F3 (NETZSCH) (**Figure S2**). The density (d) of the sintered pellets were determined by the Archimedes' method[59] which gave ~97 % of the theoretical density. κ of the pellets was then determined by the relationship of $\kappa = DC_pd$. The room-temperature Hall carrier concentration and carrier mobility (μ) were determined by a homemade apparatus using four-probe contact method with the vanderpauw technique under a reversible magnetic field of 1.5 T.

Structural and compositional characterizations

The phase and compositional analyses of the sintered pellets were carried out by X-ray diffraction (XRD) with Cu Kα (λ = 1.5418 Å) radiation in a Bruker D8 diffractometer. Scanning electron microscopy (SEM, JEOL 6610, operated at 20 kV) with energy-dispersive X-ray spectroscopy (EDS) and Hitachi's unique 200 kV aberration-corrected transmission electron microscopy (TEM, HF 5000, operated at 200 kV) were used to investigate the morphology, structure and composition of the sintered pellets. Focused ion beam (FEI-SCIOS FIB) was used to prepare thin lamella for nanoscale TEM characterization.

Computational details of band structure and density of states calculation

We employed first-principles density functional theory (DFT) to investigate the effect of In/Ag atomic substitutions on the electronic structures of SnTe. The on-site disorders due to atomic substitutions were considered using the coherent potential approximation (CPA). We utilized the Korringa-Kohn-Rostocker (KKR) Green function formalism in the atomic sphere approximation (ASA) as implemented in the AkaiKKR code. The Perdew-Burke-Ernzerhof parameterization of the generalized gradient approximation was used for the exchange-correlation functional.[60] The supercell approach widely adopted in previous studies considered an ordered distribution of dopants, i.e., an ordered alloy.[61] The calculated band structure depends sensitively on the precise distribution pattern of dopants in the matrix. The CPA method has several advantages over the supercell approach. Firstly, the fractional atomistic occupation number allows one to simulate alloys with arbitrary doping concentrations by the same computational effort. Secondly, because the same primitive cell is used in simulating pristine and doped systems, the effects of dopants can be obtained by a direct comparison of the resulting band structures. Lastly, the CPA method is built upon the electronic Green's functions. The scatterings encountered by electrons due to the dopant-matrix hybridizations, such as the electrons in the resonant state, are manifested as the broadening and distortion in the calculated spectra functions. Benchmark calculations show that the band structure of pristine SnTe obtained by the KKR-ASA method matches well with the conventional plane-wave-pseudopotential method. SnTe possesses a rock-salt face centered cubic (FCC) structure with the room-temperature lattice parameter of a = 6.32 Å. Two empty spheres per unit cell were added. The self-consistent potential was calculated using a 6×6×6 k-mesh with a tiny imaginary energy (10^{-6} Ry).

Conflicts of interest

There are no conflicts to declare.

Acknowledgements

This work was financially supported by the Australian Research Council. Z.G.C. thanks the USQ start‐up grant and strategic research grant. R.M. thanks The University of Queensland for the International Postgraduate Research Scholarship (IPRS) and UQ Centennial Scholarship for his PhD program. Microscopy Australia is acknowledged for providing characterization facilities.

Notes and references

1. W. Li, L. Zheng, B. Ge, S. Lin, X. Zhang, Z. Chen, Y. Chang and Y. Pei, *Adv. Mater.*, 2017, **29**, 1605887.
2. Q. Zhang, B. Liao, Y. Lan, K. Lukas, W. Liu, K. Esfarjani, C. Opeil, D. Broido, G. Chen and Z. Ren, *Proc. Natl. Acad. Sci.*, 2013, **110**, 13261.
3. A. Banik and K. Biswas, *J. Mater. Chem. A*, 2014, **2**, 9620.
4. G. Tan, L. D. Zhao, F. Shi, J. W. Doak, S. H. Lo, H. Sun, C. Wolverton, V. P. Dravid, C. Uher and M. G. Kanatzidis, *J. Am. Chem. Soc.*, 2014, **136**, 7006.
5. A. Banik, U. S. Shenoy, S. Saha, U. V. Waghmare and K. Biswas, *J. Am. Chem. Soc.*, 2016, **138**, 13068.
6. G. Tan, F. Shi, S. Hao, H. Chi, L.-D. Zhao, C. Uher, C. Wolverton, V. P. Dravid and M. G. Kanatzidis, *J. Am. Chem. Soc.*, 2015, **137**, 5100.
7. Y. Z. Pei, L. L. Zheng, W. Li, S. Q. Lin, Z. W. Chen, Y. Y. Wang, X. F. Xu, H. L. Yu, Y. Chen and B. H. Ge, *Adv. Electron. Mater.*, 2016, **2**, 1600019.
8. G. Tan, F. Shi, J. W. Doak, H. Sun, L.-D. Zhao, P. Wang, C. Uher, C. Wolverton, V. P. Dravid and M. G. Kanatzidis, *Energy Environ. Sci.*, 2015, **8**, 267.
9. R. Moshwan, L. Yang, J. Zou and Z.-G. Chen, *Adv. Funct. Mater.*, 2017, **27**, 1703278.
10. T. Zhu, Y. Liu, C. Fu, J. P. Heremans, J. G. Snyder and X. Zhao, *Adv. Mater.*, 2017, DOI: 10.1002/adma.201605884, 1605884.
11. G. J. Snyder and T. S. Ursell, *Phys. Rev. Lett.*, 2003, **91**, 148301.
12. L. Yang, Z.-G. Chen, M. S. Dargusch and J. Zou, *Adv. Energy Mater.*, 2018, **8**, 1701797.
13. L. Zhao, F. Y. Fei, J. Wang, F. Wang, C. Wang, J. Li, J. Wang, Z. Cheng, S. Dou and X. Wang, *Sci. Rep.*, 2017, **7**, 40436.

14. L.-D. Zhao, S.-H. Lo, J. He, H. Li, K. Biswas, J. Androulakis, C.-I. Wu, T. P. Hogan, D.-Y. Chung, V. P. Dravid and M. G. Kanatzidis, *J. Am. Chem. Soc.*, 2011, **133**, 20476.
15. C. Fu, T. Zhu, Y. Liu, H. Xie and X. Zhao, *Energy Environ. Sci.*, 2015, **8**, 216.
16. J. He, X. Tan, J. Xu, G.-Q. Liu, H. Shao, Y. Fu, X. Wang, Z. Liu, J. Xu, H. Jiang and J. Jiang, *J. Mater. Chem. A*, 2015, **3**, 19974.
17. Y. Pei, X. Shi, A. LaLonde, H. Wang, L. Chen and G. J. Snyder, *Nature*, 2011, **473**, 66.
18. Y. Pei, H. Wang and G. J. Snyder, *Adv. Mater.*, 2012, **24**, 6125.
19. T. Xiaojian, S. Hezhu, H. Tianqi, L. Guo-Qiang and R. Shang-Fen, *J. Phys. Condens. Mater.*, 2015, **27**, 095501.
20. M. Hong, Z.-G. Chen, Y. Pei, L. Yang and J. Zou, *Phys. Rev. B*, 2016, **94**, 161201.
21. J. Krez, J. Schmitt, G. Jeffrey Snyder, C. Felser, W. Hermes and M. Schwind, *J. Mater. Chem. A*, 2014, **2**, 13513.
22. J. Li, Z. Chen, X. Zhang, H. Yu, Z. Wu, H. Xie, Y. Chen and Y. Pei, *Adv. Sci.*, 2017, **4**, 1700341.
23. Y. Pei, A. D. LaLonde, N. A. Heinz, X. Shi, S. Iwanaga, H. Wang, L. Chen and G. J. Snyder, *Adv. Mater.*, 2011, **23**, 5674.
24. E. Rausch, B. Balke, T. Deschauer, S. Ouardi and C. Felser, *APL Mater.*, 2015, **3**, 041516.
25. S. N. Guin, D. S. Negi, R. Datta and K. Biswas, *J. Mater. Chem. A*, 2014, **2**, 4324.
26. B. A. Cook, M. J. Kramer, J. L. Harringa, M.-K. Han, D.-Y. Chung and M. G. Kanatzidis, *Adv. Funct. Mater.*, 2009, **19**, 1254.
27. M.-K. Han, K. Hoang, H. Kong, R. Pcionek, C. Uher, K. M. Paraskevopoulos, S. D. Mahanti and M. G. Kanatzidis, *Chem. Mater.*, 2008, **20**, 3512.
28. J.-L. Lan, Y. Liu, Y.-H. Lin, C.-W. Nan, Q. Cai and X. Yang, *Sci. Rep.*, 2015, **5**, 7783.
29. E. Quarez, K.-F. Hsu, R. Pcionek, N. Frangis, E. K. Polychroniadis and M. G. Kanatzidis, *J. Am. Chem. Soc.*, 2005, **127**, 9177.
30. L.-D. Zhao, J. He, S. Hao, C.-I. Wu, T. P. Hogan, C. Wolverton, V. P. Dravid and M. G. Kanatzidis, *J. Am. Chem. Soc.*, 2012, **134**, 16327.
31. Z.-G. Chen, G. Han, L. Yang, L. Cheng and J. Zou, *Prog. Nat. Sci.*, 2012, **22**, 535.
32. Y. Tian, M. R. Sakr, J. M. Kinder, D. Liang, M. J. MacDonald, R. L. J. Qiu, H.-J. Gao and X. P. A. Gao, *Nano Lett.*, 2012, **12**, 6492.
33. W.-X. Zhou, S. Tan, K.-Q. Chen and W. Hu, *J. Appl. Phys.*, 2014, **115**, 124308.
34. S. Bhattacharya, A. Bohra, R. Basu, R. Bhatt, S. Ahmad, K. N. Meshram, A. K. Debnath, A. Singh, S. K. Sarkar, M. Navneethan, Y. Hayakawa, D. K. Aswal and S. K. Gupta, *J. Mater. Chem. A*, 2014, **2**, 17122.
35. K. Biswas, J. He, I. D. Blum, C.-I. Wu, T. P. Hogan, D. N. Seidman, V. P. Dravid and M. G. Kanatzidis, *Nature*, 2012, **489**, 414.
36. Y. Lee, S.-H. Lo, J. Androulakis, C.-I. Wu, L.-D. Zhao, D.-Y. Chung, T. P. Hogan, V. P. Dravid and M. G. Kanatzidis, *J. Am. Chem. Soc.*, 2013, **135**, 5152.
37. L. D. Zhao, H. J. Wu, S. Q. Hao, C. I. Wu, X. Y. Zhou, K. Biswas, J. Q. He, T. P. Hogan, C. Uher, C. Wolverton, V. P. Dravid and M. G. Kanatzidis, *Energy Environ. Sci.*, 2013, **6**, 3346.
38. L.-D. Zhao, X. Zhang, H. Wu, G. Tan, Y. Pei, Y. Xiao, C. Chang, D. Wu, H. Chi, L. Zheng, S. Gong, C. Uher, J. He and M. G. Kanatzidis, *J. Am. Chem. Soc.*, 2016, **138**, 2366.
39. M. Hong, Y. Wang, T. Feng, Q. Sun, S. Xu, S. Matsumura, S. T. Pantelides, J. Zou and Z.-G. Chen, *J. Am. Chem. Soc.*, 2019, **141**, 1742.
40. M. H. Lee, D.-G. Byeon, J.-S. Rhyee and B. Ryu, *J. Mater. Chem. A*, 2017, **5**, 2235.
41. X. Shi, K. Zheng, M. Hong, W. Liu, R. Moshwan, Y. Wang, X. Qu, Z.-G. Chen and J. Zou, *Chem. Sci.*, 2018, **9**, 7376.
42. R. Moshwan, X.-L. Shi, W.-D. Liu, Y. Wang, S. Xu, J. Zou and Z.-G. Chen, *ACS Appl. Energy Mater.*, 2019, **2**, 2965.
43. C. W. Li, J. Ma, H. B. Cao, A. F. May, D. L. Abernathy, G. Ehlers, C. Hoffmann, X. Wang, T. Hong, A. Huq, O. Gourdon and O. Delaire, *Phys. Rev. B*, 2014, **90**, 214303.
44. G. A. S. Ribeiro, L. Paulatto, R. Bianco, I. Errea, F. Mauri and M. Calandra, *Phys. Rev. B*, 2018, **97**, 014306.
45. W. Liu, X. Shi, R. Moshwan, M. Hong, L. Yang, Z.-G. Chen and J. Zou, *Sustainable Mater.Tech.*, 2018, **17**, e00076.
46. X. Shi, A. Wu, W. Liu, R. Moshwan, Y. Wang, Z.-G. Chen and J. Zou, *ACS Nano*, 2018, **12**, 11417.
47. M. Hong, Y. Wang, S. Xu, X. Shi, L. Chen, J. Zou and Z.-G. Chen, *Nano Energy*, 2019, **60**, 1.
48. R. Moshwan, W.-D. Liu, X.-L. Shi, Y.-P. Wang, J. Zou and Z.-G. Chen, *Nano Energy*, 2019, **65**, 104056.
49. R. Moshwan, X.-L. Shi, W.-D. Liu, L. Yang, Y. Wang, M. Hong, G. Auchterlonie, J. Zou and Z.-G. Chen, *ACS Appl. Mater. Interf.*, 2018, **10**, 38944.
50. A. Banik and K. Biswas, *J. Solid State Chem.*, 2016, **242**, 43.
51. A. Banik, U. S. Shenoy, S. Anand, U. V. Waghmare and K. Biswas, *Chem. Mater.*, 2015, **27**, 581.
52. D. K. Bhat and S. Shenoy U, *J. Phys. Chem. C*, 2017, **121**, 7123.
53. L. Wang, X. Tan, G. Liu, J. Xu, H. Shao, B. Yu, H. Jiang, S. Yue and J. Jiang, *ACS Energy Lett.*, 2017, **2**, 1203.
54. X. Tan, G. Liu, J. Xu, X. Tan, H. Shao, H. Hu, H. Jiang, Y. Lu and J. Jiang, *J. Materiomics*, 2018, **4**, 62.
55. D. K. Bhat and U. S. Shenoy, *Mater. Today Phys.*, 2018, **4**, 12.
56. J. Q. Li, N. Yang, S. M. Li, Y. Li, F. S. Liu and W. Q. Ao, *J. Electron. Mater.*, 2018, **47**, 205.
57. H.-S. Kim, Z. M. Gibbs, Y. Tang, H. Wang and G. J. Snyder, *APL Mater.*, 2015, **3**, 041506.
58. M. Thesberg, H. Kosina and N. Neophytou, *Phys. Rev. B*, 2017, **95**, 125206.
59. B. Mason, *Geol. Foren. Stockh. Forh.*, 1944, **66**, 27.
60. J. P. Perdew, K. Burke and M. Ernzerhof, *Phys. Rev. Lett.*, 1996, **77**, 3865.
61. J. Tang, B. Gao, S. Lin, J. Li, Z. Chen, F. Xiong, W. Li, Y. Chen and Y. Pei, *Adv. Funct. Mater.*, 2018, **28**, 1803586.

Supporting information

Outstanding thermoelectric properties in solvothermal-synthesized $Sn_{1-3x}In_xAg_{2x}Te$ micro-crystals through defect engineering and band tuning

Raza Moshwan[a,e], Wei-Di Liu[a], Xiao-Lei Shi[b], Sun Qiang[a], Han Gao[a], Yun-Peng Wang[d], Jin Zou[a,c,**], and Zhi-Gang Chen[b,a*]

[a]*Materials Engineering, The University of Queensland, St Lucia, QLD 4072, Australia*

[b]*Centre for Future Materials, The University of Southern Queensland, Springfield Central, QLD 4300, Australia*

[c]*Centre for Microscopy and Microanalysis, The University of Queensland, St Lucia, QLD 4072, Australia*

[d]*School of Physics and Electronics, Hunan Key Laboratory for Super-micro structure and Ultrafast Process, Central South University, 932 South Lushan Road, Changsha, P. R. China*

[e]*University of Creative Technology Chittagong, Chandgaon Police Station, 1084, Shah Amanat Bridge Connecting Road, Chittagong 4212, Bangladesh*

E-mail:

**zhigang.chen@usq.edu.au, zhigang.chen@uq.edu.au*

***j.zou@uq.edu.au*

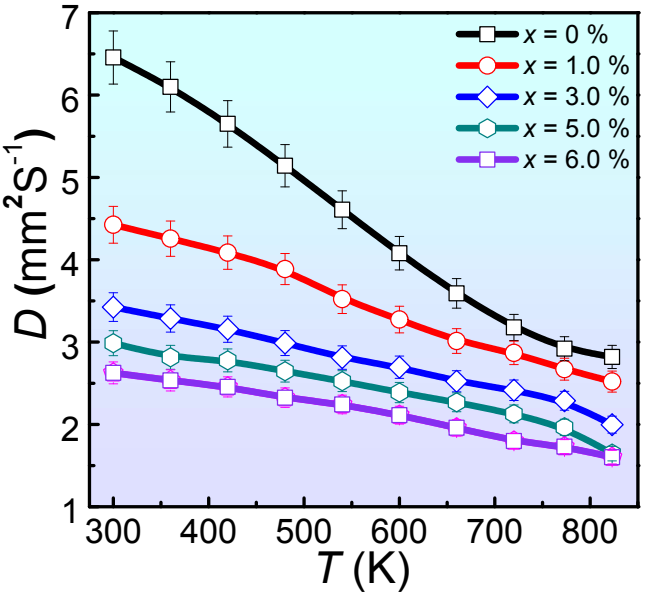

Figure S1. Thermal diffusivity *D* as a function of temperature for different $Sn_{1-3x}In_xAg_{2x}Te$.

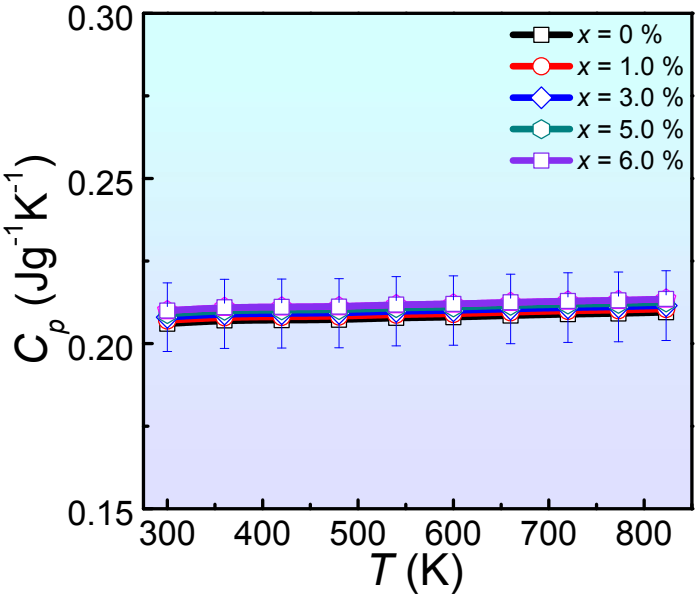

Figure S2. Specific heat (C_p) of $Sn_{1-3x}In_xAg_{2x}Te$ samples

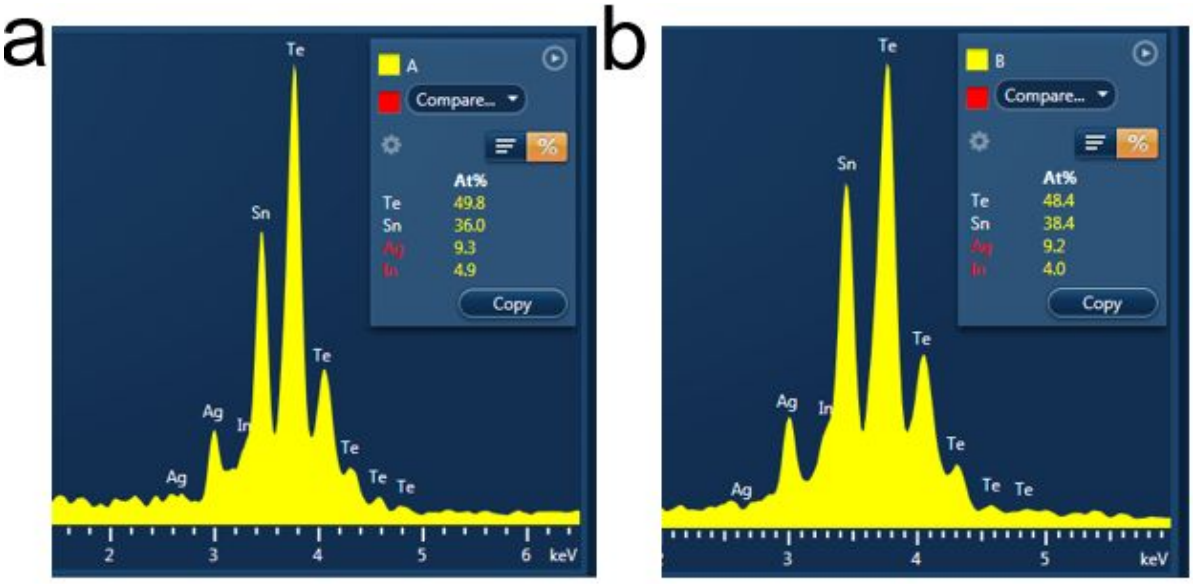

Figure S3. EDS spectrum and compositional analyses of spot A and B from **Figure 1e.**

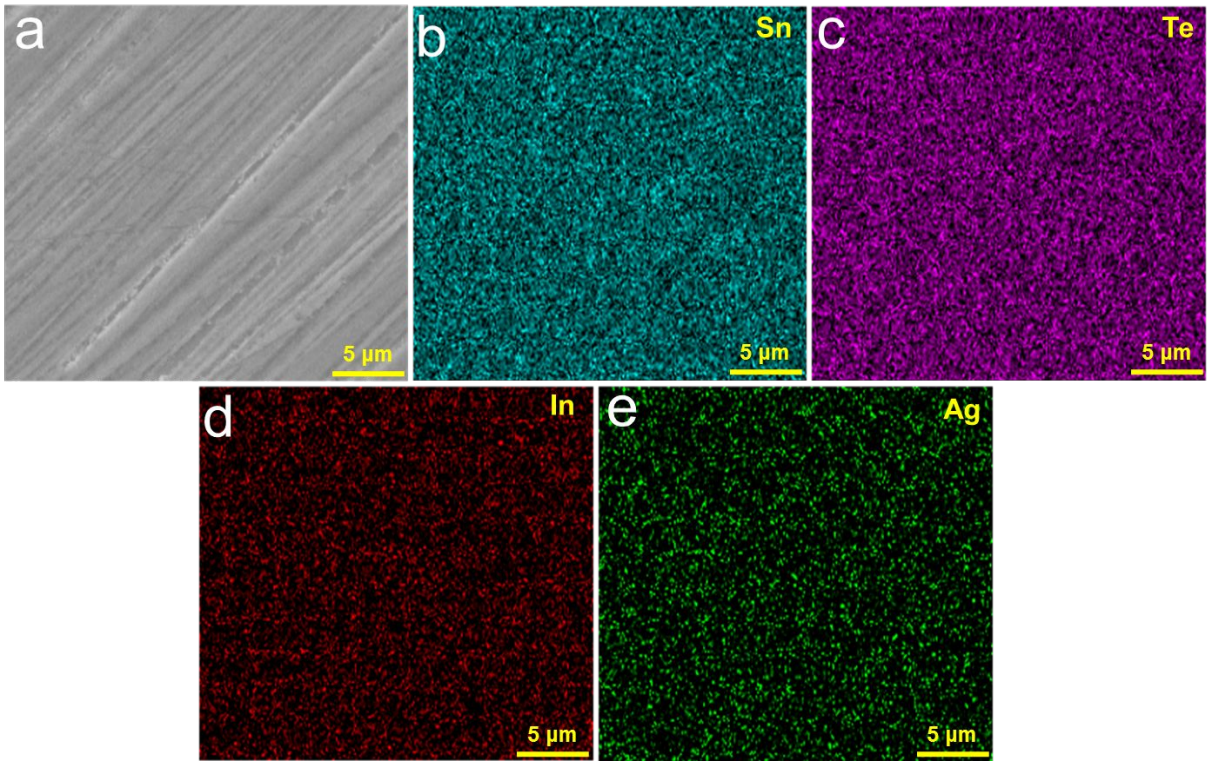

Figure S4. (a) A typical SEM image of the sintered $Sn_{0.85}In_{0.05}Ag_{0.10}Te$ pellet and (b-e) Corresponding EDS elemental map data of Sn, Te, In and Ag.

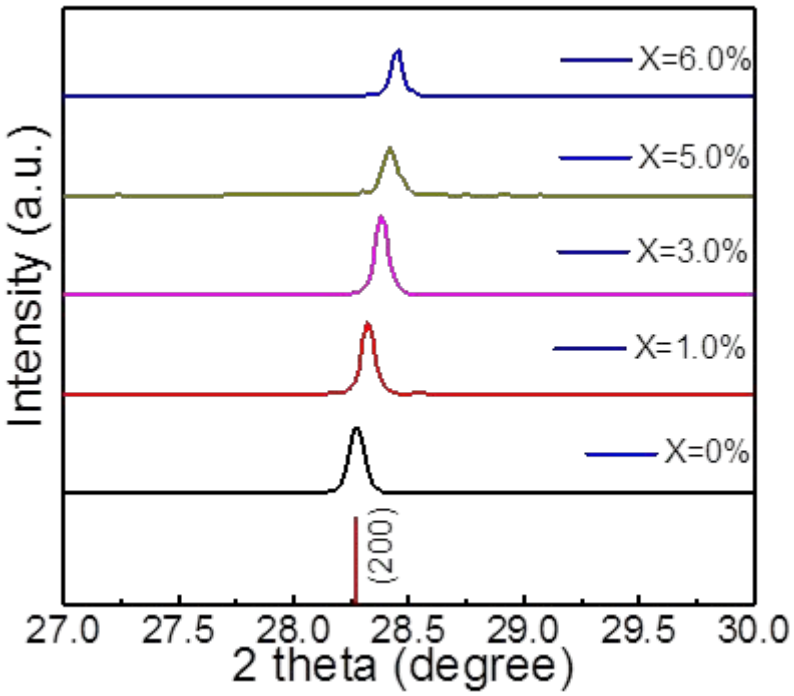

Figure S5. Extended (200) peak of **Figure 2**a shows peaks are shifting towards higher angle demonstrating the lattice shrinkage of the lattice.

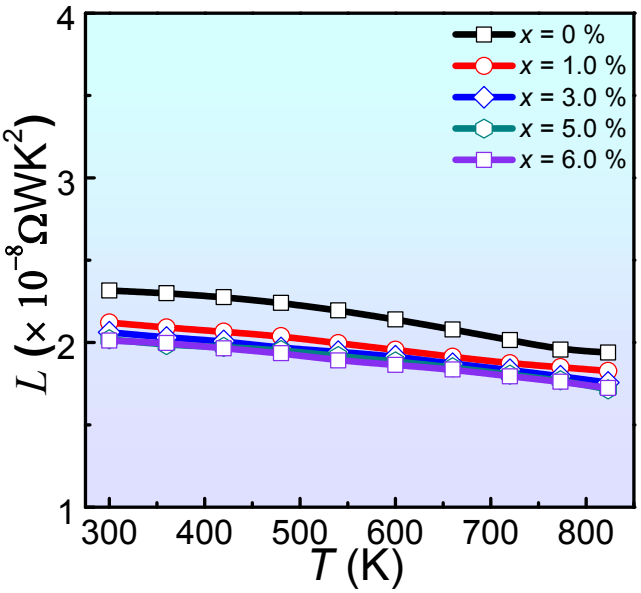

Figure S6. Calculated Lorenz number *L* as function of temperature of $Sn_{1-3x}In_xAg_{2x}Te$.